

1
2
3
4
5
6
7
8
9
10
11
12
13
14
15
16
17
18
19

Arctic rift system driven by a giant stagnant slab

Genti Toyokuni^{1*} and Dapeng Zhao¹

¹ Department of Geophysics, Graduate School of Science, Tohoku University, Sendai 980-8578,
Japan

Submitted to *Geophysical Research Letters* in June 2021

*Corresponding author:

Genti Toyokuni

E-mail: toyokuni@tohoku.ac.jp

ORCID ID: 0000-0003-3786-207X

Key Points:

- High-resolution *P* wave tomography of the whole mantle beneath the circum-Arctic region is obtained.
- A giant stagnant slab with subducted oceanic ridge is revealed below the 660-km discontinuity beneath Canada and Greenland.
- Division between Canada and Greenland at 63–35 Ma might be induced by complex tensional field associated with the stagnant slab.

20 **Abstract**

21 A detailed 3-D tomographic model of the whole mantle beneath the circum-Arctic region is
22 obtained by applying an updated global tomography method to a large amount of *P*-wave arrival
23 time data. Our model clearly shows the subducted Izanagi and Farallon slabs penetrating into the
24 lower mantle beneath Eurasia and North America, respectively. In the region from Canada to
25 Greenland, a giant stagnant slab lying below the 660-km discontinuity is revealed. Because this
26 slab has a texture that seems to be due to subducted oceanic ridges, the slab might be composed
27 of the Izanagi, Farallon, Kula and Vancouver slabs that had subducted during ~80–20 Ma.
28 During that period, a complex rift system represented by division between Canada and
29 Greenland was developed. The oceanic ridge subduction and hot upwelling in the big mantle
30 wedge above the stagnant slab caused a tensional stress field, which might have induced these
31 complex tectonic events.

32 **Plain Language Summary**

33 The circum-Arctic region has many clues for understanding global-scale tectonics and revolution
34 of the Earth. Seismic tomography is a well-established method for obtaining 3-D images of the
35 underground structure by inverting a large number of seismic wave arrival times. We obtain
36 detailed tomographic images of the whole mantle beneath the circum-Arctic region by using an
37 updated global tomography method. Our high-resolution results clearly show the subducted
38 Izanagi and Farallon slabs penetrating into the lower mantle beneath Eurasia and North America,
39 respectively. In the region from Canada to Greenland, a giant stagnant slab lying below the 660-
40 km discontinuity with a total length of ~4,000 km is revealed. Because this slab has a texture that
41 seems to be due to subducted oceanic ridges, the slab might be composed of the Izanagi, Farallon,
42 Kula and Vancouver slabs that had subducted during ~80–20 Ma. During that period, a complex

43 rift system represented by division between Canada and Greenland was developed. The oceanic
44 ridge subduction and hot upwelling in the big mantle wedge above the stagnant slab caused a
45 tensional stress field, which might have induced these complex tectonic events.

46 **1. Introduction**

47 The underground structure beneath the circum-Arctic region ([Figure 1](#)) is a frontier of our
48 geoscientific knowledge that has been poorly understood compared to other regions of the
49 Northern Hemisphere. Especially in recent years, the underground structure and tectonics of this
50 area have received widespread attention because, for example, a possibility of resource mining
51 has increased due to decrease in ice in the Arctic Ocean, and the underground temperature affects
52 melting of the Greenland Ice Sheet and global sea level rise ([Martos et al., 2018](#); [Toyokuni et al.,](#)
53 [2020a](#)).

54 One of the major mysteries of tectonics in this area is the existence of the Canadian
55 Arctic Rift System (CARS). Its latest activity was the Eureka Rifting Episode (ERE),
56 symbolized by the division between Greenland and Canada and complex movement of the
57 Canadian Arctic Archipelago (CAA), which took place between 63 and 35 Ma ([Gion et al.,](#)
58 [2017](#)). It is known that this division began in the Labrador Sea on the south side and propagated
59 to Baffin Bay on the north side. Simultaneously, flood basalts erupted widely in West Greenland,
60 Davis Strait, and Baffin Island ([Chalmers et al., 1995](#); [Larsen et al., 2016](#)). Traditionally, these
61 events were thought to be induced by the rising Iceland plume ([Gerlings et al., 2009](#); [Gill et al.,](#)
62 [1992](#)). However, from reconstruction of the plume track ([Peace et al., 2017](#)), geothermal heat
63 flow estimation ([Artemieva, 2019](#); [Martos et al., 2018](#)), and seismic velocity structure ([Toyokuni](#)
64 [et al., 2020a](#)), it is unlikely that the Iceland plume passed through this area. [Peace et al. \(2017\)](#)

65 proposed a far field tectonic force as an alternative mechanism that caused the division, but they
66 did not mention its direct cause.

67 In Greenland, a seismograph network had recently been developed with international
68 cooperation, and high-quality data have been accumulated (Clinton et al., 2014; Toyokuni et al.,
69 2014). Structures beneath Greenland, Iceland, and surrounding regions have been intensively
70 investigated by seismic waveform analyses (Kumar et al., 2007; Mordret et al., 2016; Toyokuni
71 et al., 2015, 2018, 2021a), surface wave tomography (Antonijevic & Lees, 2018; Darbyshire et
72 al., 2004, 2018; Levshin et al., 2017; Mordret, 2018; Pilidou et al., 2004; Pourpoint et al., 2018),
73 body wave tomography (Toyokuni & Zhao, 2021; Toyokuni et al., 2020a, 2020b), and full-wave
74 tomography (Rickers et al., 2013). However, the previous studies targeting the whole circum-
75 Arctic region focused on the structure shallower than 700 km depth (Jakovlev et al., 2012;
76 Lebedev et al., 2017). Seismic tomography, especially body-wave tomography, is a well-
77 established and high-resolution method for investigating deep structure of the Earth. To
78 investigate the relationship between tectonics of the circum-Arctic region and large-scale
79 geodynamic events such as plate subduction and hot mantle plume that occurred or are occurring
80 in surrounding regions, we need to study the whole mantle structure with high resolution over a
81 vast horizontal scale. In this study we exploit the updated global tomography method that can
82 reveal the whole mantle structure beneath a specific area with high resolution (Toyokuni et al.,
83 2020b; Zhao et al., 2017) to execute multiple computations for different areas, and to obtain
84 detailed panoramic tomography by stitching the individual images together. The purpose of this
85 study is to investigate the cause of ERE from a tectonic viewpoint using our novel tomographic
86 model.

87 2. Data & Method

88 We apply the multiscale global tomography method by [Zhao et al. \(2017\)](#), which adopts a
89 fine 3-D grid for the target region and a coarse 3-D grid for the surrounding regions of the globe.
90 Thus, the structural model beneath the target region can be obtained with high resolution while
91 saving computational resources. Applying this method to the Izu-Bonin subduction zone, [Zhao et
92 al. \(2017\)](#) investigated the detailed 3-D structure of the subducted Pacific slab where the 2015
93 Bonin deep earthquake ($M7.9$; depth ~ 680 km) took place. This method was also applied to
94 investigate the whole mantle structure beneath Greenland ([Toyokuni et al., 2020b](#)) and Southeast
95 Asia ([Zhao et al., 2021](#)).

96 We apply a coordinate transformation that moves the center of the target area to
97 (longitude, latitude) = $(90^\circ, 0^\circ)$ to treat high latitude areas by nearly rectangular grid distributions
98 ([Takenaka et al., 2017](#); [Toyokuni et al., 2020a, 2020b](#)). To clarify the relationship between
99 tectonic phenomena with a large horizontal scale such as plate subduction and a hot mantle
100 plume, our target covers the entire region north of $\sim 30^\circ\text{N}$ latitude. The computation cost is
101 reduced by performing independent calculations with 12 different regions and superimposing the
102 results to obtain a final tomographic model.

103 [Table S1](#) shows the central location (longitude and latitude) for each of the 12 regions.
104 Each calculation is performed for a region covering the longitude range from 60° to 120° and the
105 latitude range from -30° to 30° after the coordinate transformation. In the vicinity of the North
106 Pole, where only a few seismic stations and earthquakes exist, calculations are performed in two
107 regions rotated by $\sim 40^\circ$ around the North Pole to reduce the distortion of the results due to the
108 grid arrangement (Regions 1 and 2). In addition, 10 regions with different positions and angles
109 are further arranged around them (Regions 3–12) ([Figure S1](#)).

110 Data are collected from the ISC-EHB catalog at the International Seismological Centre
111 (ISC) website (<http://www.isc.ac.uk/>) and further selected for our analysis. The P , pP , and PP
112 (Figure S2) arrival times from 170,435 earthquakes are selected. To make the hypocentral
113 distribution uniform, the entire crust and mantle are divided into small cubic blocks, and only
114 one earthquake with the largest number of data in each block is extracted. We extract as many
115 earthquakes as possible that occurred inside the target region, by adopting finer blocks inside the
116 target region and coarser blocks outside it. The block size is changed for each calculation to
117 roughly homogenize the number of earthquakes and data used in each calculation (Table S1 and
118 Figures S3–S14). Table S1 also shows the numbers of seismic stations and arrival time data used.

119 We set a fine 3-D grid with a lateral grid interval of 55.6 km (a great circle distance of
120 0.5° on the surface) in the target region, and a coarse 3-D grid with a lateral grid interval of
121 222.39 km (a great circle distance of 2.0° on the surface) outside the target region. The vertical
122 grid intervals inside and outside the target region are also different (see Table S2). Theoretical
123 traveltimes are calculated using a 3-D ray tracing method (Zhao, 2004) that simultaneously uses
124 the pseudo-bending scheme (Um & Thurber, 1987) and Snell's law. The IASP91 model (Kennett
125 & Engdahl, 1991) is taken to be the 1-D initial V_p model for the tomographic inversion (Figure
126 S15). The tomographic inversion is conducted using the LSQR algorithm (Paige & Saunders,
127 1982) with damping and smoothing regularizations (Zhao, 2004). The optimal values of the
128 damping and smoothing parameters are adopted according to the previous studies (Toyokuni et
129 al., 2020b; Zhao et al., 2017, 2021).

130 To reduce the influence of boundary of the target region, the edges of each tomographic
131 model obtained by the individual inversion for the 12 regions are cut off, and we extract only the
132 results 4° inside the longitude and latitude ranges of the target region. Then we rearrange the 12

133 Vp models according to the coordinate system of Region 1, and take weight average using the
134 ray hit count. As a result, the final tomographic model is obtained from the surface to the core-
135 mantle boundary (CMB) beneath the region north of $\sim 30^\circ\text{N}$ latitude. Such jointing of multiple
136 tomography results has been adopted by previous studies targeting a wide area (e.g., [Jakovlev et](#)
137 [al., 2012](#)).

138 **3. Results**

139 Map view images of the tomographic results are shown in [Figures 2 and S16](#). For the
140 areas where some of the 12 regions overlap, the ray hit count (HC) in each region is averaged,
141 and the regions where average $\text{HC} < 20$ ([Figure S17](#)) are masked in white. At a depth of 160 km,
142 high-Vp anomalies are visible in forearc regions, and low-Vp and high-Vp anomalies appear in
143 the eastern and western parts of North America, respectively, which is consistent with previous
144 tomographic models (e.g., [Golos et al., 2018](#)). At a depth of 400 km, a low-Vp zone beneath the
145 Iceland and Azores hotspots is visible. At a depth of 800 km, a wide range of high-Vp from
146 North America to North Eurasia and low-Vp in surrounding regions are prominent. At a depth of
147 1500 km, no distinctive features are visible, but at a depth of 2100 km, the “Greenland plume”
148 ([Toyokuni et al., 2020b](#)) and low-Vp beneath the western Pacific are prominent. At a depth of
149 2880 km, there is a marked increase in high-Vp and low-Vp amplitudes near CMB.

150 Vertical cross-sections of our model ([Figure 3](#)) clearly image the subducting Farallon slab
151 beneath the North American continent, which has penetrated into the lower mantle ([Figure 3a](#)).
152 Beneath the Eurasian continent, the Izanagi slab penetrating into the lower mantle is also clearly
153 resolved ([Figure 3c](#)). As a plate becomes thicker and heavier as it moves away from the ridge
154 axis, it is likely to fall into the lower mantle after stagnation around the 660-km discontinuity.
155 The penetration of the Farallon slab into the lower mantle has already been revealed by many

156 tomographic studies (e.g., Schmid et al., 2002; Zhao, 2004). On the other hand, penetration of
157 the Izanagi slab was only predicted by studies based on mantle convection modeling (Peng &
158 Liu, 2021). This is the first time that the penetrating Izanagi slab is clearly imaged by seismic
159 tomography. In Figure 3a, we can also see low- V_p , which appears to be a hot plume rising from
160 the CMB below Hawaii toward the west coast of North America.

161 Beneath Canada and Greenland, located between the two penetrating slabs, a high- V_p
162 anomaly lies at depths of ~800 km (Figure 3b). While this high- V_p anomaly can be seen almost
163 near the surface at the western end, it deepens toward the east and continues for a total length of
164 ~4,000 km. This feature reminds us of a giant stagnant slab. Vertical cross-sections with a finer
165 grid interval beneath Canada and Greenland are shown in Figure S18. Comparisons with other
166 tomographic models (Amaru, 2007; Lu et al., 2019; Ritsema et al., 2011; Simmons et al., 2010,
167 2012) show that the main features in Figure 3a are robust, but those in Figures 3b and 3c vary
168 depending on the model (Figures S19–S21).

169 The resolution of the tomographic images is investigated using multiple synthetic tests
170 including the checkerboard resolution test (CRT) (Humphreys & Clayton, 1988; Zhao et al.,
171 2017) and restoring resolution test (RRT) (Toyokuni et al., 2021b; Zhao et al., 2017).
172 Specifically, the following four input V_p models are constructed and tested (Toyokuni et al.,
173 2020b): (1) CRT1: the checkerboard has a lateral grid interval of 278 km (a great circle distance
174 of 2.5° on the surface) inside the study region, (2) CRT2: the lateral grid interval is 167 km (a
175 great circle distance of 1.5° on the surface) inside the study region, (3) RRT1: highlighting the
176 pattern of the obtained tomographic result, (4) RRT2: the same as RRT1 but a regional
177 rectangular high- V_p anomaly is added at depths of 650-800 km. Figures S22–S25 show the
178 recovery rate of CRT (Toyokuni et al., 2020b) and the RRT results. The CRT results show that

179 the resolution in our study region is 1.5° in the lateral direction and the distances comparable to
180 the vertical grid interval in the depth direction for regions with average $HC \geq 20$. The RRT
181 results also show that the pattern of tomographic results can be recovered very well. [Figures](#)
182 [S26–S28](#) also show the reliability of main features in [Figure 3](#).

183 **4. Discussion**

184 The map view at a depth of 800 km ([Figures 2c and 4a](#)) shows that the amplitude of high-
185 V_p anomalies in the region from Canada to the Arctic Ocean is not uniform, and that the
186 amplitude changes like stripes. Comparison of RRT1 and RRT2 results indicates that this feature
187 is reliable ([Figure S29](#)). Overlapping the results of plate reconstruction by [Müller et al. \(2019\)](#),
188 these stripes are coincident with the oceanic ridge axis subducted approximately normal to the
189 trench axis. Specifically, the regions with the lineament of weaker high- V_p amplitudes are
190 consistent well with the ridge axis between the Farallon and Izanagi plates subducted during
191 160–85 Ma, and the ridge axis at the boundary of the Kula and Vancouver plates subducted
192 during 85–20 Ma ([Figure 4 and Video S1](#)). Therefore, we consider that the lineament of weak
193 high- V_p anomalies indicates the subducted oceanic ridge where the slab is thin, and the
194 lineament with strong high- V_p zones on its both sides indicates the part where the slabs are
195 relatively thick. This correspondence reinforces the possibility that the high- V_p anomaly beneath
196 this region reflects a stagnant slab.

197 According to a recent study ([Domeier et al., 2017](#)), the traditionally considered Kula plate
198 is a complex of the western Kronos plate and the eastern Kula plate, with subduction of the Kula
199 plate beneath the Kronos plate forming a westward slope. In this case, the subduction axis of the
200 Kula plate runs almost parallel to the eastern Kula–Farallon ridge, which better corresponds to

201 the two parallel lineaments of weak high-Vp zones beneath North America in our tomographic
202 results.

203 The plate near the ridge axis is young and less heavy, so it is easy to stagnant at a depth
204 in the mantle. Furthermore, the trench axis due to the subduction of this area continued to retreat
205 (Figure 4), providing an environment where the slab stagnation was likely to occur. When the
206 slab is light enough, it does not fall into the lower mantle but keeps to stagnate until it is
207 thermally assimilated with its surroundings (Nakakuki et al., 2010).

208 Above the long stagnant slab, a huge wedge-shaped mantle is formed, which is called the
209 Big Mantle Wedge (BMW) and was firstly found in East Asia (Zhao, 2004; Lei & Zhao, 2005;
210 Zhao et al., 2009). In the BMW, subduction-driven corner flow and fluids from deep dehydration
211 reactions of the stagnant Pacific slab in the mantle transition zone result in upwelling of hot and
212 wet asthenospheric materials, causing intraplate volcanism and continental rift systems in East
213 Asia. The BMW above the subducted Farallon/Nazca slab also caused Cenozoic intraplate
214 magmatism in Patagonia (Navarrete et al., 2020). Referring to these previous studies, combining
215 our tomography and the plate reconstruction results, we propose that the BMW above the
216 stagnant slab in the circum-Arctic region caused the continental breakup during ERE and the
217 accompanying volcanism in West Greenland, Davis Strait, and Baffin Island in Tertiary.

218 Unlike East Asia and Patagonia, the stagnant slab in the present study region is
219 characterized by the oceanic ridge axis subducted nearly orthogonal to the trench axis. Because
220 the oceanic plates diverge to both sides of the ridge axis, when the ridge is subducted, a tensional
221 stress field is likely to form in the trench-parallel direction in the overlying plate. Combined with
222 the dominant trench-normal tensional stress regime formed by upwelling flows in the BMW, the

223 upper plate in this area is likely to be dominated by tensional stresses oriented in various
224 directions, which might have induced the complex division of CAA (Figure 5).

225 The root of this stagnant slab is located between the Cascadia and Alaska subduction
226 zones in North America, where currently only the strike-slip Queen Charlotte Fault exists, and
227 the subduction has already ceased. After the ERE, CARS became inactive and the entire rift
228 system is now moving as part of the North American Plate. This fact also supports our proposal
229 that CARS was induced by the stagnant slab. Toyokuni et al. (2020b) discovered the Greenland
230 plume ascending from CMB beneath Greenland, which rises up eastward and is connected with
231 Svalbard and Jan Mayen. The direction of plume fluttering is opposite to the moving direction of
232 the plate on which Greenland is placed. However, considering that the stagnant slab may obstruct
233 the upwelling flow, the strange flowline of the Greenland plume (Toyokuni et al., 2020b) can be
234 well explained.

235 **Acknowledgments**

236 We are grateful to Drs. Dean Childs, Kevin Nikolaus, Kent Anderson, Masaki Kanao,
237 Yoko Tono, Seiji Tsuboi, Robin Abbott, Kathy Young, Drew Abbott, Silver Williams, Jason
238 Hebert, Tetsuto Himeno, Susan Whitley, Orlando Leone, Akram Mostafanejad, Kirsten Arnell,
239 and other staff members at GLISN, IRIS/PASSCAL, CH2M HILL Polar Services, and
240 Norlandair for their contributions to the field operations in Greenland. This work was partially
241 supported by research grants from Japan Society for the Promotion of Science (Nos. 18K03794,
242 24403006, 23224012, 19H01996, and 26241010). The GMT (Wessel et al., 2013) and GPlates
243 (Müller et al., 2018) software packages are used in this study. The SubMachine website
244 (<https://www.earth.ox.ac.uk/~smachine/cgi/index.php>) (Hosseini et al., 2018) is used to generate
245 cross sections of other tomography models. Arrival-time data are downloaded from the ISC

246 (<http://www.isc.ac.uk/>). Archiving of data from this study is underway through Zenodo.
247 Currently these data can be seen in Supporting Information for review purposes.

248 **Author contributions**

249 Conceptualization: Genti Toyokuni, Dapeng Zhao

250 Data curation: Genti Toyokuni

251 Formal analysis: Genti Toyokuni

252 Methodology: Genti Toyokuni, Dapeng Zhao

253 Resources: Genti Toyokuni, Dapeng Zhao

254 Visualization: Genti Toyokuni

255 Writing – original draft: Genti Toyokuni

256 Writing – review & editing: Genti Toyokuni, Dapeng Zhao

257 **References**

258 Amaru, M. L. (2007). Global travel time tomography with 3-D reference models. Doctoral thesis,
259 Utrecht University. <https://dspace.library.uu.nl/handle/1874/314949>

260 Antonijevic, S. K., & Lees, J. M. (2018). Effects of the Iceland plume on Greenland's
261 lithosphere: New insights from ambient noise tomography. *Polar Science*, 17, 75–82.
262 <https://doi.org/10.1016/j.polar.2018.06.004>

263 Artemieva, I. M. (2019). Lithosphere thermal thickness and geothermal heat flux in Greenland
264 from a new thermal isostasy method. *Earth-Science Reviews*, 188, 469–481.
265 <https://doi.org/10.1016/j.earscirev.2018.10.015>

- 266 Chalmers, J. A., Larsen, L. M., & Pedersen, A. K. (1995). Widespread Palaeocene volcanism
267 around the northern North Atlantic and Labrador Sea: evidence for a large, hot, early
268 plume head. *Journal of the Geological Society*, 152, 965–969.
269 <https://doi.org/10.1144/GSL.JGS.1995.152.01.14>
- 270 Clinton, J. F., Nettles, M., Walter, F., Anderson, K., Dahl-Jensen, T., Giardini, D., Govoni, A.,
271 Hanka, W., Lasocki, S., Lee, W. S., McCormack, D., Mykkeltveit, S., Stutzmann, E., &
272 Tsuboi, S. (2014). Seismic network in Greenland monitors Earth and ice system. *Eos,*
273 *Transactions, American Geophysical Union*, 95(2), 13–24.
274 <https://doi.org/10.1002/2014EO020001>
- 275 Darbyshire, F. A., Dahl-Jensen, T., Larsen, T. B., Voss, P. H., & Joyal, G. (2018). Crust and
276 uppermost-mantle structure of Greenland and the Northwest Atlantic from Rayleigh wave
277 group velocity tomography. *Geophysical Journal International*, 212(3), 1546–1569.
278 <https://doi.org/10.1093/gji/ggx479>
- 279 Darbyshire, F. A., Larsen, T. B., Mosegaard, K., Dahl-Jensen, T., Gudmundsson, Ó., Bach, T., et
280 al. (2004). A first detailed look at the Greenland lithosphere and upper mantle, using
281 Rayleigh wave tomography. *Geophysical Journal International*, 158(1), 267–286.
282 <https://doi.org/10.1111/j.1365-246X.2004.02316.x>
- 283 Domeier, M., Shephard, G. E., Jakob, J., Gaina, C., Doubrovine, P. V., & Torsvik, T. H., (2017).
284 Intraoceanic subduction spanned the Pacific in the Late Cretaceous–Paleocene. *Science*
285 *Advances*, 3(11), eaao2303. <https://doi.org/10.1126/sciadv.aao2303>
- 286 Gerlings, J., Funck, T., Jackson, H. R., Loudon, K. E., & Klingelhöfer, F., 2009. Seismic
287 evidence for plume-derived volcanism during formation of the continental margin in

288 southern Davis Strait and northern Labrador Sea. *Geophysical Journal International*, 176,
289 980–994. <https://doi.org/10.1111/j.1365-246X.2008.04021.x>

290 Gill, R. C. O., Pedersen, A. K., & Larsen, J. G., 1992. Tertiary picrites in West Greenland:
291 melting at the periphery of a plume? In B. C. Storey, T. Alabaster, & R. J. Pankhurst
292 (Eds.), *Magmatism and the Causes of Continental Break-up* (Vol. 68, pp. 335–348).
293 London: Geological Society of London. <https://doi.org/10.1144/GSL.SP.1992.068.01.21>

294 Gion, A. M., Williams, S. E., & Müller, R. D. (2017). A reconstruction of the Eurekan Orogeny
295 incorporating deformation constraints, *Tectonics*, 36, 304–320.
296 <https://doi.org/10.1002/2015TC004094>

297 Golos, E. M., Fang, H., Yao, H., Zhang, H., Burdick, S., Vernon, F., Schaeffer, A., Lebedev, S.,
298 & van der Hilst, R. D. (2018). Shear wave tomography beneath the United States using a
299 joint inversion of surface and body waves. *Journal of Geophysical Research: Solid Earth*,
300 123, 5169–5189. <https://doi.org/10.1029/2017JB014894>

301 Hosseini, K., Matthews, K. J., Sigloch, K., Shephard, G. E., Domeier, M., & Tsekhmistrenko, M.
302 (2018), SubMachine: Web-Based tools for exploring seismic tomography and other
303 models of Earth's deep interior. *Geochemistry, Geophysics, Geosystems*, 19(5), 1464-
304 1483. <https://doi.org/10.1029/2018GC007431>

305 Humphreys, E., & Clayton, R. W. (1988). Adaptation of back projection tomography to seismic
306 travel time problems. *Journal of Geophysical Research*, 93(B2), 1073–1085.
307 <https://doi.org/10.1029/JB093iB02p01073>

- 308 Jakovlev, A. V., Bushenkova, N. A., Koulakov, I. Yu., & Dobretsov, N. L. (2012). Structure of
309 the upper mantle in the Circum-Arctic region from regional seismic tomography. *Russian*
310 *Geology and Geophysics*, 53(10), 963–971. <https://doi.org/10.1016/j.rgg.2012.08.001>
- 311 Kennett, B. L. N., & Engdahl, E. R. (1991). Traveltimes for global earthquake location and phase
312 identification. *Geophysical Journal International*, 105, 429–465.
313 <https://doi.org/10.1111/j.1365-246X.1991.tb06724.x>
- 314 Kumar, P., Kind, R., Priestley, K., & Dahl-Jensen, T. (2007). Crustal structure of Iceland and
315 Greenland from receiver function studies. *Journal of Geophysical Research: Solid Earth*,
316 112(B3), B03301. <https://doi.org/10.1029/2005JB003991>
- 317 Larsen, L. M., Pedersen, A. K., Tegner, C., Duncan, R. A., Hald, N., & Larsen, J. G. (2016). Age
318 of Tertiary volcanic rocks on the West Greenland continental margin: volcanic evolution
319 and event correlation to other parts of the North Atlantic Igneous Province. *Geological*
320 *Magazine*, 153, 487–511. <https://doi.org/10.1017/S0016756815000515>
- 321 Lebedev, S., Schaeffer, A. J., Fulla, J., & Pease, V. (2017). Seismic tomography of the Arctic
322 region: inferences for the thermal structure and evolution of the lithosphere. *Geological*
323 *Society, London, Special Publications*, 460, 419–440. <https://doi.org/10.1144/SP460.10>
- 324 Lei, J., & Zhao, D. (2005). P-wave tomography and origin of the Changbai intraplate volcano in
325 Northeast Asia. *Tectonophysics*, 397(3–4), 281–295.
326 <https://doi.org/10.1016/j.tecto.2004.12.009>
- 327 Levshin, A. L., Shen, W., Barmin, M. P., & Ritzwoller, M. H. (2017). Surface wave studies of
328 the Greenland upper lithosphere using ambient seismic noise.
329 <https://pdfs.semanticscholar.org/977c/ce2101b7f9b384d38e9b051bf289a7277b54.pdf>

- 330 Lu, C., Grand, S. P., Lai, H., & Garnero, E. J. (2019). TX2019slab: A new P and S tomography
331 model incorporating subducting slabs. *Journal of Geophysical Research: Solid Earth*, 124,
332 11549–11567. <https://doi.org/10.1029/2019JB017448>
- 333 Martos, Y. M., Jordan, T. A., Catalán, M., Jordan, T. M., Bamber, J. L., & Vaughan, D. G.
334 (2018). Geothermal heat flux reveals the Iceland hotspot track underneath Greenland.
335 *Geophysical Research Letters*, 45, 8214–8222. <https://doi.org/10.1029/2018GL078289>
- 336 Mordret, A. (2018). Uncovering the Iceland hot spot track beneath Greenland. *Journal of*
337 *Geophysical Research: Solid Earth*, 123, 4922–4941.
338 <https://doi.org/10.1029/2017JB015104>
- 339 Mordret, A., Mikesell, T. D., Harig, C., Lipovsky, B. P., & Prieto, G. A. (2016). Monitoring
340 southwest Greenland's ice sheet melt with ambient seismic noise. *Science Advances*,
341 2(5), e1501538. <http://dx.doi.org/10.1126/sciadv.1501538>
- 342 Müller, R. D., Cannon, J., Qin, X., Watson, R. J., Gurnis, M., Williams, S., et al. (2018).
343 GPLates: Building a virtual Earth through deep time. *Geochemistry, Geophysics,*
344 *Geosystems*, 19, 2243–2261. <https://doi.org/10.1029/2018GC007584>
- 345 Müller, R. D., Zahirovic, S., Williams, S. E., Cannon, J., Seton, M., Bower, D. J., Tetley, M. G.,
346 Heine, C., Le Breton, E., Liu, S., Russell, S. H. J., Yang, T., Leonard, J., & Gurnis, M.
347 (2019). A global plate model including lithospheric deformation along major rifts and
348 orogens since the Triassic. *Tectonics*, 38(6), 1884–1907.
349 <https://doi.org/10.1029/2018TC005462>

- 350 Nakakuki, T., Tagawa, M., & Iwase, Y. (2010). Dynamical mechanisms controlling formation
351 and avalanche of a stagnant slab. *Physics of the Earth and Planetary Interiors*, 183, 309–
352 320. <https://doi.org/10.1016/j.pepi.2010.02.003>
- 353 Navarrete, C., Gianni, G., Massafiero, G., & Butler, K. (2020). The fate of the Farallon slab
354 beneath Patagonia and its links to Cenozoic intraplate magmatism, marine transgressions
355 and topographic uplift. *Earth-Science Reviews*, 210, 103379.
356 <https://doi.org/10.1016/j.earscirev.2020.103379>
- 357 Paige, C. C., & Saunders, M. A. (1982). LSQR, An algorithm for sparse linear equations and
358 sparse least squares. *ACM Transactions on Mathematical Software (TOMS)*, 8(1), 43–71.
359 <https://doi.org/10.1145/355984.355989>
- 360 Peace, A. L., Foulger, G. R., Schiffer, C., & McCaffrey, K. J. (2017). Evolution of Labrador
361 Sea–Baffin Bay: Plate or plume processes? *Geoscience Canada*, 44(3), 91–102.
362 <https://doi.org/10.12789/geocanj.2017.44.120>
- 363 Peng, D., & Liu, L. (2021). A newly discovered Late-Cretaceous East Asian flat slab explains its
364 unique lithospheric structure and tectonics. <https://doi.org/10.1002/essoar.10506583.1>
- 365 Pilidou, S., Priestley, K., Gudmundsson, Ó., & Debayle, E. (2004). Upper mantle S - wave speed
366 heterogeneity and anisotropy beneath the North Atlantic from regional surface wave
367 tomography: The Iceland and Azores plumes. *Geophysical Journal International*, 159,
368 1057–1076. <https://doi.org/10.1111/j.1365-246X.2004.02462.x>
- 369 Pourpoint, M., Anandkrishnan, S., Ammon, C. J., & Alley, R. B. (2018). Lithospheric structure
370 of Greenland from ambient noise and earthquake surface wave tomography. *Journal of*

- 371 *Geophysical Research: Solid Earth*, 123, 7850–7876.
372 <https://doi.org/10.1029/2018JB015490>
- 373 Rickers, F., Fichtner, A., & Trampert, J. (2013). The Iceland–Jan Mayen plume system and its
374 impact on mantle dynamics in the North Atlantic region: Evidence from full-waveform
375 inversion. *Earth and Planetary Science Letters*, 367, 39–51.
376 <https://doi.org/10.1016/j.epsl.2013.02.022>
- 377 Ritsema, J., Deuss, A., van Heijst, H. J., & Woodhouse, J. H. (2011). S40RTS: a degree-40
378 shear-velocity model for the mantle from new Rayleigh wave dispersion, teleseismic
379 traveltimes and normal-mode splitting function measurements. *Geophysical Journal*
380 *International*, 184, 1223–1236. <https://doi.org/10.1111/j.1365-246X.2010.04884.x>
- 381 Schmid, C., Goes, S., van der Lee, S., & Giardini, D. (2002). Fate of the Cenozoic Farallon slab
382 from a comparison of kinematic thermal modeling with tomographic images. *Earth and*
383 *Planetary Science Letters*, 204(1–2), 17–32. [https://doi.org/10.1016/S0012-](https://doi.org/10.1016/S0012-821X(02)00985-8)
384 [821X\(02\)00985-8](https://doi.org/10.1016/S0012-821X(02)00985-8)
- 385 Simmons, N. A., Forte, A. M., Boschi, V., & Grand, S. P. (2010). GyPSuM: A joint tomographic
386 model of mantle density and seismic wave speeds. *Journal of Geophysical Research:*
387 *Solid Earth*, 115(B12), B12310. <https://doi.org/10.1029/2010JB007631>
- 388 Simmons, N. A., Myers, S. C., Johannesson, G., & Matzel, E. (2012). LLNL-G3Dv3: Global P
389 wave tomography model for improved regional and teleseismic travel time prediction.
390 *Journal of Geophysical Research: Solid Earth*, 117, B10302.
391 <https://doi.org/10.1029/2012JB009525>

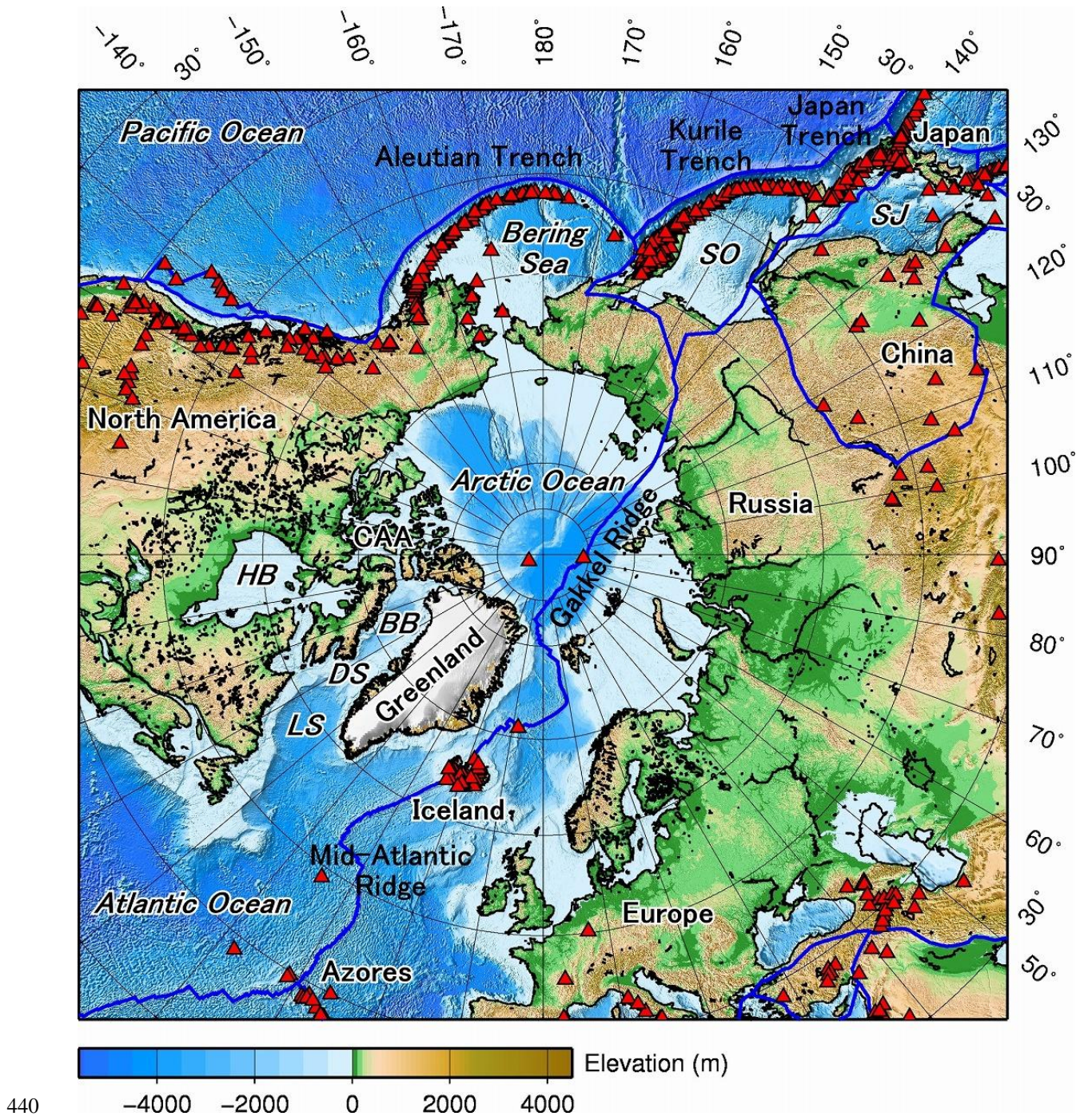
- 392 Takenaka, H., Komatsu, M., Toyokuni, G., Nakamura, T., & Okamoto, T. (2017). Quasi-
393 Cartesian finite-difference computation of seismic wave propagation for a three-
394 dimensional sub-global model. *Earth, Planets and Space*, 69, 67.
395 <https://doi.org/10.1186/s40623-017-0651-1>
- 396 Toyokuni, G., & Zhao, D. (2021). P wave tomography for 3-D radial and azimuthal anisotropy
397 beneath Greenland and surrounding regions. <https://doi.org/10.1002/essoar.10506588.1>
- 398 Toyokuni, G., Kanao, M., Tono, Y., Himeno, T., Tsuboi, S., Childs, D., Anderson, K., &
399 Takenaka, H. (2014). Monitoring of the Greenland ice sheet using a broadband
400 seismometer network: the GLISN project. *Antarctic Record*, 58(1), 1–18.
401 <http://doi.org/10.15094/00009722>
- 402 Toyokuni, G., Komatsu, M., & Takenaka, H. (2021a). Estimation of seismic attenuation of the
403 Greenland Ice Sheet using 3-D waveform modeling. *Journal of Geophysical Research:*
404 *Solid Earth*. <https://doi.org/10.1029/2021JB021694>
- 405 Toyokuni, G., Matsuno, T., & Zhao, D. (2020a). P wave tomography beneath Greenland and
406 surrounding regions: 1. Crust and upper mantle. *Journal of Geophysical Research: Solid*
407 *Earth*, 125, e2020JB019837. <https://doi.org/10.1029/2020JB019837>
- 408 Toyokuni, G., Matsuno, T., & Zhao, D. (2020b). P wave tomography beneath Greenland and
409 surrounding regions: 2. Lower mantle. *Journal of Geophysical Research: Solid Earth*,
410 125, e2020JB019839. <https://doi.org/10.1029/2020JB0198379>
- 411 Toyokuni, G., Takenaka, H., Kanao, M., Tsuboi, S., & Tono, Y. (2015). Numerical modeling of
412 seismic waves for estimating the influence of the Greenland ice sheet on observed
413 seismograms. *Polar Science*, 9(1), 80–93. <https://doi.org/10.1016/j.polar.2014.12.001>

- 414 Toyokuni, G., Takenaka, H., Takagi, R., Kanao, M., Tsuboi, S., Tono, Y., Childs, D., & Zhao, D.
415 (2018). Changes in Greenland ice bed conditions inferred from seismology. *Physics of*
416 *the Earth and Planetary Interiors*, 277, 81–98. <https://doi.org/10.1016/j.pepi.2017.10.010>
- 417 Toyokuni, G., Zhao, D., & Chen, K. H. (2021b). Structural control on the 2018 and 2019 Hualien
418 earthquakes in Taiwan. *Physics of the Earth and Planetary Interiors*, 312, 106673.
419 <https://doi.org/10.1016/j.pepi.2021.106673>
- 420 Um, J., & Thurber, C. (1987). A fast algorithm for two-point seismic ray tracing. *Bulletin of the*
421 *Seismological Society of America*, 77(3), 972–986.
- 422 Wessel, P., Smith, W. H. F., Scharroo, R., Luis, J., & Wobbe, F. (2013). Generic Mapping Tools:
423 Improved Version Released. *Eos, Transactions, American Geophysical Union*, 94(45),
424 409. <https://doi.org/10.1002/2013EO450001>
- 425 Zhao, D. (2004). Global tomographic images of mantle plumes and subducting slabs: Insight into
426 deep Earth dynamics. *Physics of the Earth and Planetary Interiors*, 146(1–2), 3–34.
427 <https://doi.org/10.1016/j.pepi.2003.07.032>
- 428 Zhao, D., Fujisawa, M., & Toyokuni, G. (2017). Tomography of the subducting Pacific slab and
429 the 2015 Bonin deepest earthquake (Mw 7.9). *Scientific Reports*, 7, 44487.
430 <https://doi.org/10.1038/srep44487>
- 431 Zhao, D., Tian, Y., Lei, J., Liu, L., & Zheng, S. (2009). Seismic image and origin of the
432 Changbai intraplate volcano in East Asia: Role of big mantle wedge above the stagnant
433 Pacific slab. *Physics of the Earth and Planetary Interiors*, 173(3–4), 197–206.
434 <https://doi.org/10.1016/j.pepi.2008.11.009>

435 Zhao, D., Toyokuni, G., & Kurata, K. (2021). Deep mantle structure and origin of Cenozoic
436 intraplate volcanoes in Indochina, Hainan and South China Sea. *Geophysical Journal*
437 *International*, 225(1), 572–588. <https://doi.org/10.1093/gji/ggaa605>

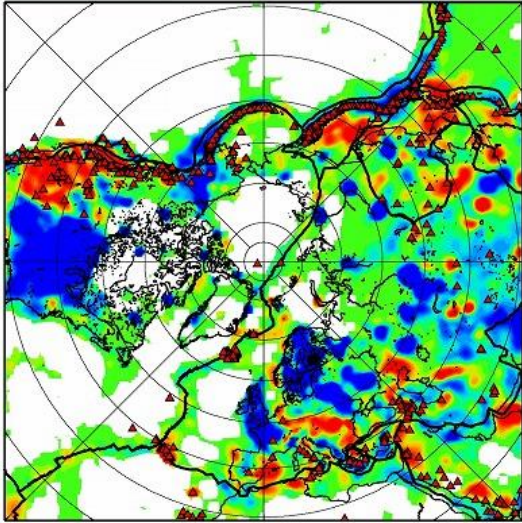
438

439

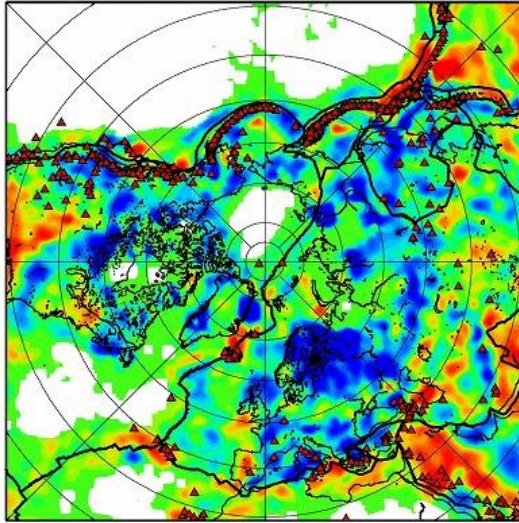


441 **Figure 1.** Map of the circum-Arctic region. The color scale for the topography is shown at the
442 bottom. White color denotes the Greenland Ice Sheet. Red triangles: active volcanoes; thick blue
443 lines: plate boundaries. CAA = Canadian Arctic Archipelago; BB = Baffin Bay; DS = Davis
444 Strait; HB = Hudson Bay; LS = Labrador Sea; SJ = Sea of Japan; SO = Sea of Okhotsk.
445

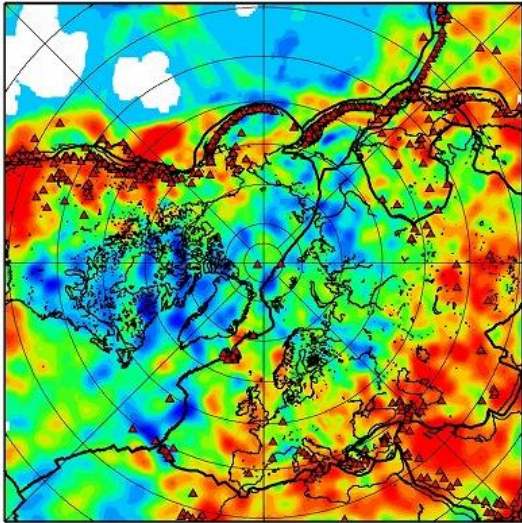
(a) 160 km



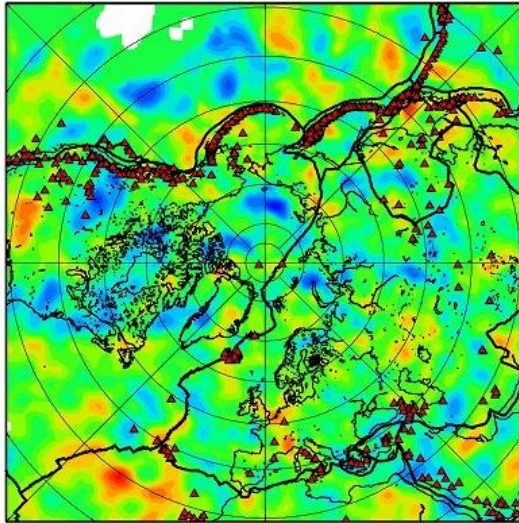
(b) 400 km



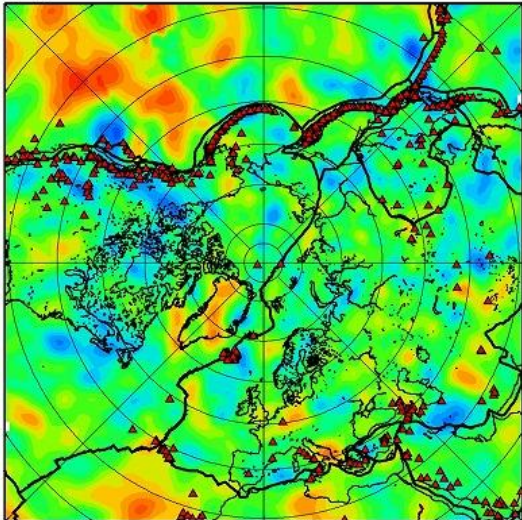
(c) 800 km



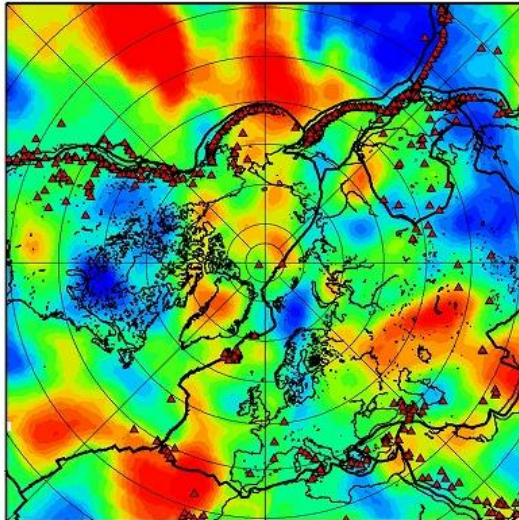
(d) 1500 km



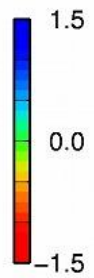
(e) 2100 km



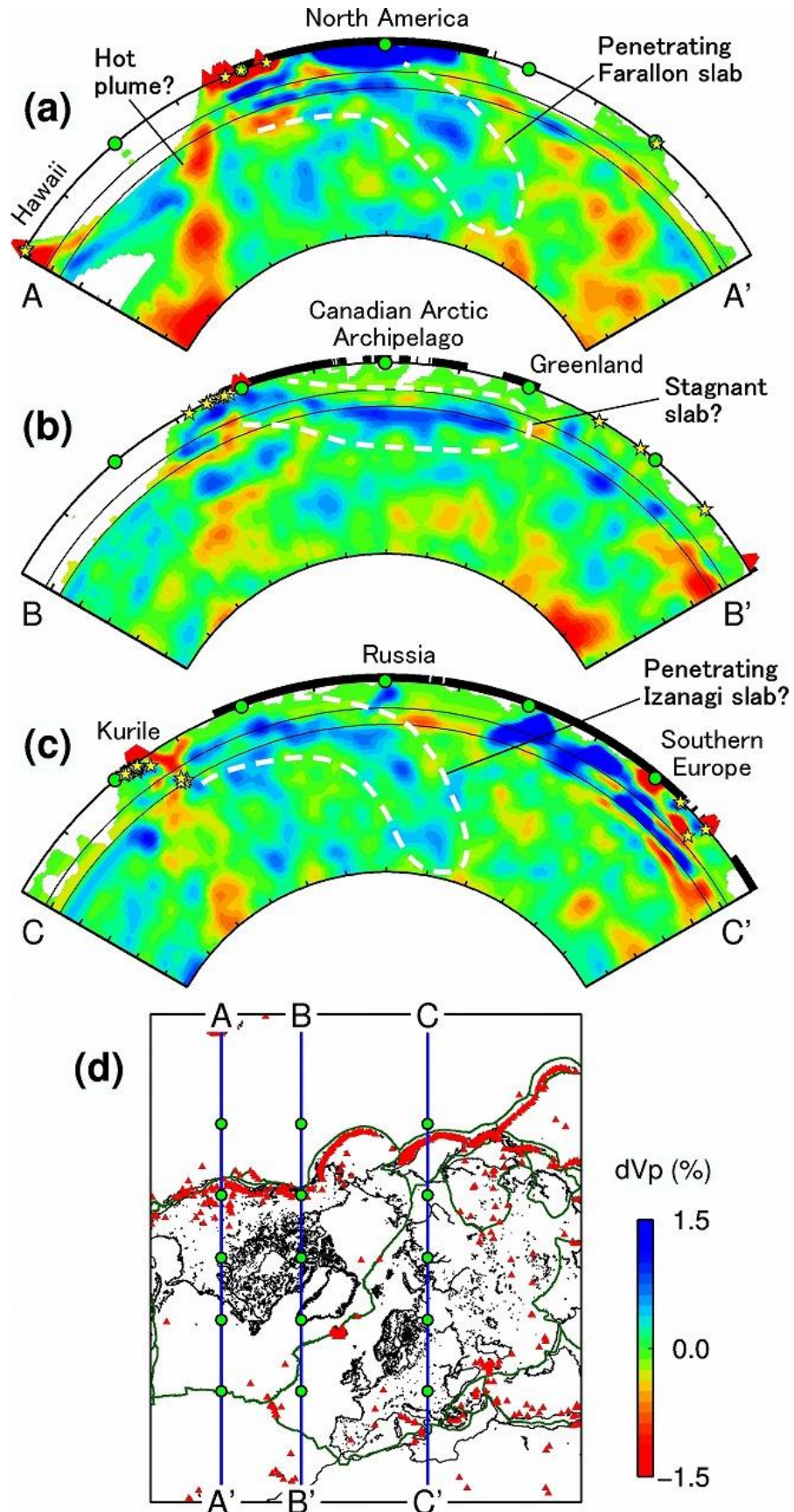
(f) 2880 km



dVp (%)

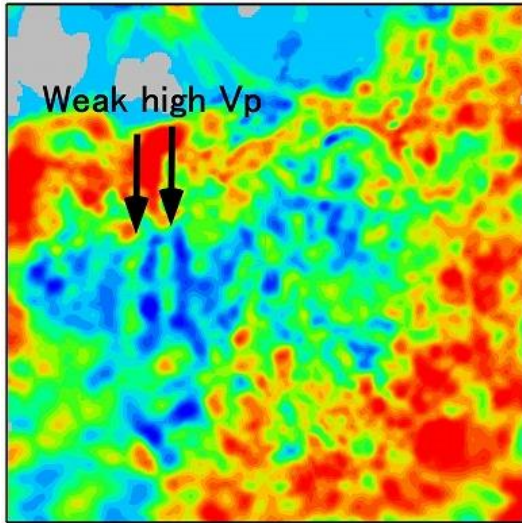


447 **Figure 2.** Map views of V_p tomography at six depths obtained by this study. The layer depth is
448 shown above each map. The blue and red colors denote high and low V_p perturbations,
449 respectively, whose scale (in %) is shown on the right. Areas with average hit counts < 20 are
450 masked in white. Red triangles: active volcanoes; thick black lines: plate boundaries.

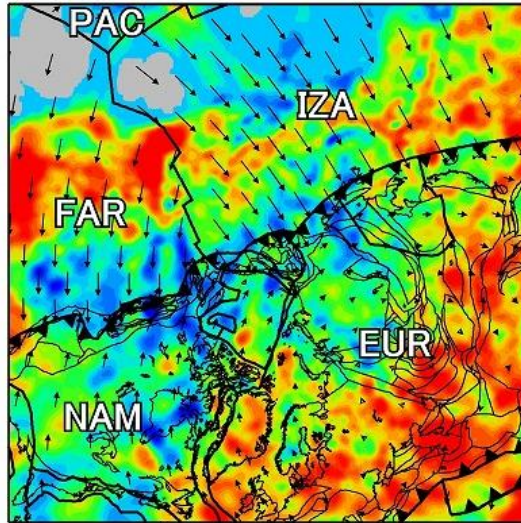


452 **Figure 3.** Vertical cross sections of Vp tomography showing main tectonic features. **(a–c)**
453 Vertical cross sections along three profiles as shown on the map **(d)**. The scale for Vp
454 perturbation (in %) is shown on the right. The 410 and 660 km discontinuities are shown in black
455 solid lines. The thick black lines on the surface denote land areas. Areas with average hit counts
456 < 20 are masked in white. Red triangles: active volcanoes existing within $\pm 2^\circ$ of each profile;
457 yellow stars: large earthquakes ($M \geq 6$) that occurred during 1964–2015 within $\pm 2^\circ$ of each
458 profile; green circles: points dividing the section equidistantly using the central angle of the earth,
459 which correspond to those in **(d)**. In the map **(d)**, red triangles: active volcanoes; thick green
460 lines: plate boundaries.

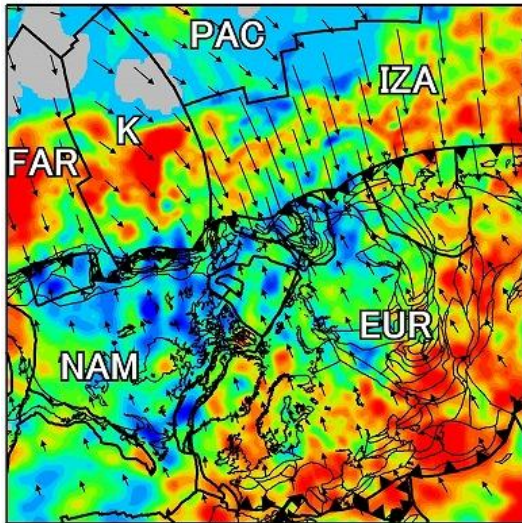
(a) Tomography (D=800 km)



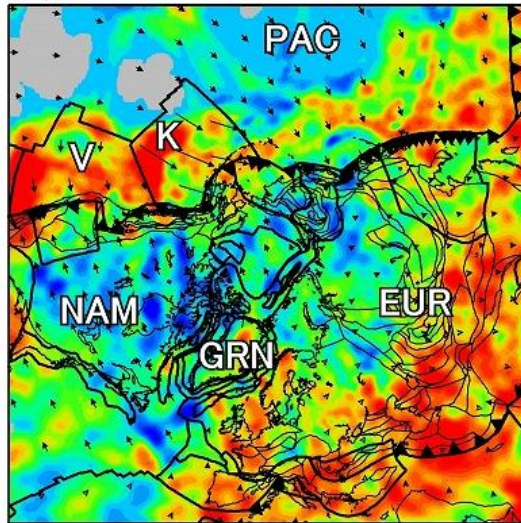
(b) 110 Ma



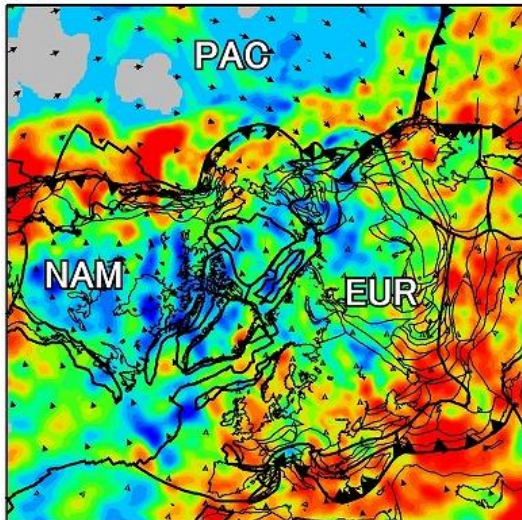
(c) 80 Ma



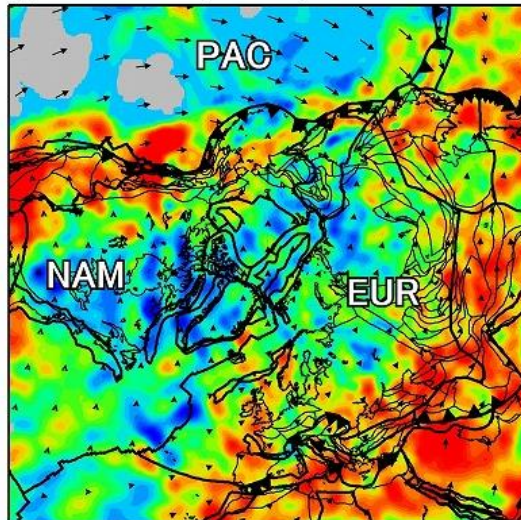
(d) 50 Ma



(e) 30 Ma



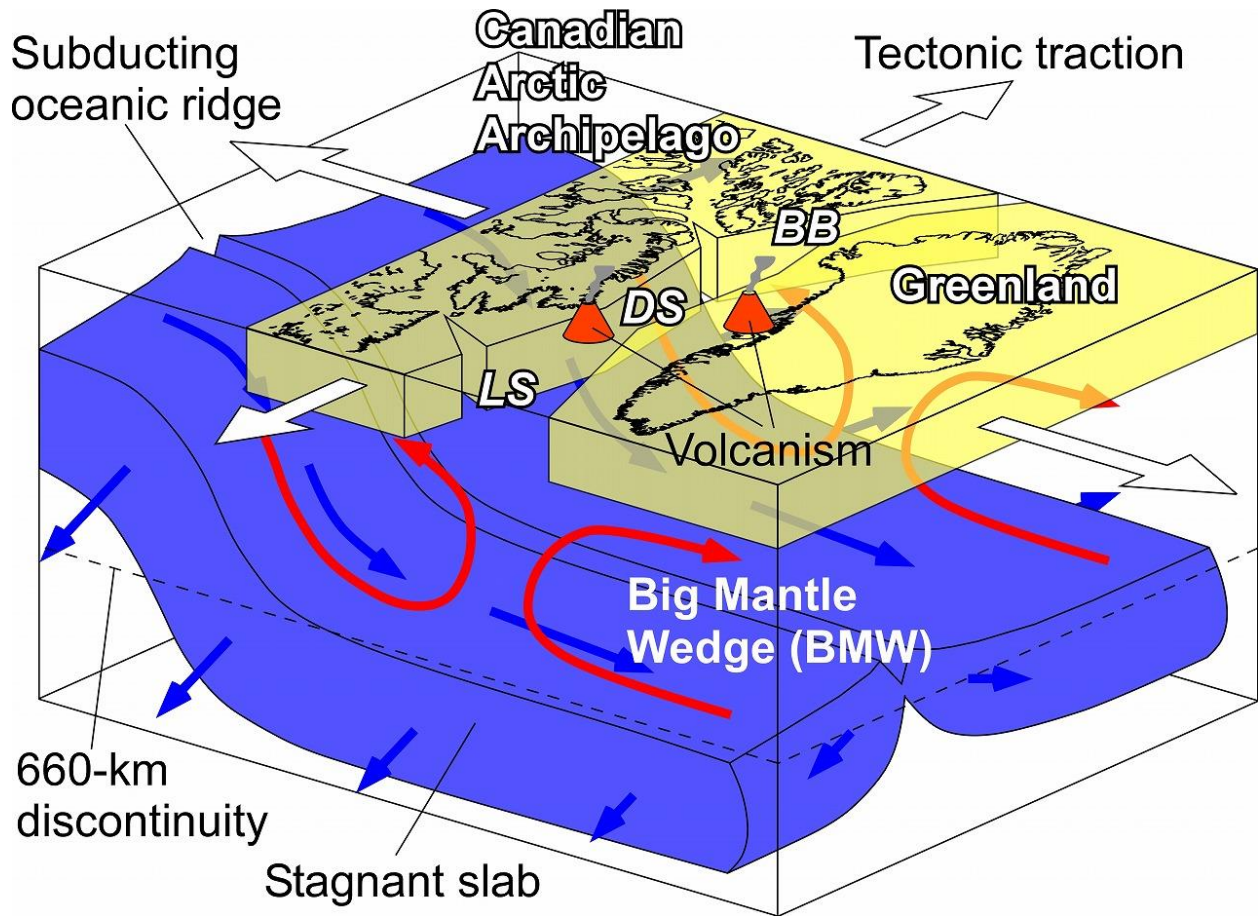
(f) Present (0 Ma)



462 **Figure 4. (a)** Map views of Vp tomography at a depth of 800 km (same as in [Figure 2c](#)) and **(b–**
463 **f)** comparison with plate reconstructions ([Müller et al., 2019](#)) from 110 Ma to the present day.
464 The scale for Vp perturbation (in %) is shown on the right. In **(a)**, thick arrows show locations of
465 weak high Vp lineaments. In **(b–f)**, the age of reconstruction is shown above each panel. Black
466 toothed lines delineate subduction zones, and other black lines denote mid-ocean ridges and
467 transform faults. The length and azimuth of each arrow denote the speed and direction of the
468 absolute plate motion, respectively. The scale for plate speed is shown on the right. EUR =
469 Eurasian Plate; FAR = Farallon Plate; GRN = Greenland Plate; IZA = Izanagi Plate; K = Kula
470 Plate; NAM = North American Plate; PAC = Pacific Plate; V = Vancouver Plate.

471

472



473

474 **Figure 5.** Schematic diagram showing a possible mechanism of the division between Greenland
 475 and Canada and tearing of crust beneath the Canadian Arctic Archipelago revealed by this study.
 476 The subducting slab with oceanic ridge becomes stagnant beneath the 660-km discontinuity
 477 beneath Canada and Greenland. The red arrows indicate upwelling of hot asthenospheric
 478 materials due to convective circulation process in the Big Mantle Wedge. The blue arrows
 479 indicate subduction and divergence directions of the subducted slab. The white arrows on the
 480 surface indicate tectonic traction, whose length conceptually indicates the traction strength. BB =
 481 Baffin Bay; DS = Davis Strait; LS = Labrador Sea.